A general approach for the direct fabrication of metal oxide-based electrocatalysts for efficient bifunctional oxygen electrodes

W. Jie, H. L. Xin

To be published in "SUSTAINABLE ENERGY & FUELS"

June 2017

Center for Functional Nanomaterials

Brookhaven National Laboratory

U.S. Department of Energy

USDOE Office of Science (SC), Basic Energy Sciences (BES) (SC-22)

DISCLAIMER

A General Approach for the Direct Fabrication of Metal Oxide-Based Electrocatalysts for Efficient Bifunctional Oxygen Electrodes

Jie Wang,[a] Zexing Wu,[a] Lili Han,[c] Cuijuan Xuan,[a] Jing Zhu,[a] Weiping Xiao,[a] Jianzhong Wu,[a] Huolin L. Xin[b] and Deli Wang[a,*]

A simple one-pot synthetic strategy for the general preparation of nitrogen doped carbon supported metal/metal oxides (Co@CoO/NDC, Ni@NiO/NDC and MnO/NDC) derives from (Ethylenediamine)tetraacetic acid (EDTA) complexing function is developed. EDTA serves not only as resource to tune the morphology in terms of the complex constant for M-EDTA, but also nitrogen and oxygen source for the nitrogen doping and metal oxides formation, respectively. When the materials are used as electrocatalysts for oxygen electrode reaction, Co@CoO/NDC-700 and MnO/NDC-700 show superior electrocatalytic activity towards oxygen reduction reaction (ORR), while Co@CoO/NDC-700 and Ni@NiO/NDC-700 exhibit excellent oxygen evolution reaction (OER) activities. Taking together, the resultant Co@CoO/NDC-700 exhibits the best catalytic activity with favorable reaction kinetics and durability as a bi-functional catalyst for ORR and OER, which is much better than the other two catalysts, Pt/C and Ir/C. Moreover, as air electrode for a homemade zinc-air battery, Co@CoO/NDC-700 shows superior cell performance with highest power density of 192.1 mW cm^{-2}, lowest charge-discharge overpotential and high charge-discharge durability over 100 h.

Introduction

Exploring advanced high-performance materials for renewable energy storage and conversion devices is appealing due to the shortage of fossil fuels and environmental pollution. Fuel cells and metal-air batteries are recognized as environmentally friendly power equipment with high-energy density[1, 2]. However, the sluggish kinetics of the oxygen reduction reaction (ORR) on the cathode has long been one of the main obstacles to the further development of proton exchange membrane fuel cells (PEMFCs)[3-5], direct methanol fuel cells (DMFCs)[6, 7] and metal-air batteries[8-10]. Typical for a metal-air battery, the bifunctional catalytic performance for ORR and oxygen evolution reaction (OER) in the cathode is appealing[11, 12]. Among various catalysts, Pt-based catalysts are, at present, renowned as the best electrocatalysts for ORR[13-15]. However, platinum is scarce, precious, vulnerable to be poisoned by some small molecules such as CO, H_2S, etc.[16-18] and also not an ideal electrocatalyst for OER. Although Ir-based catalysts exhibit superior OER performance, the prohibitive cost, the terrible shortage of iridium and relative poor ORR performance restricted the bifunctional development[19, 20]. Thus, it is of great importance to develop non-precious bi-functional catalysts for reversible metal-air battery with high ORR and OER activity[21-26].

Recently, *3d*-transition metal-based materials have been arising increasing interest for the ORR and OER in alkaline media[27-32]. Compared with precious metal catalysts, transition metal resources are less expensive, more abundant, geographically ubiquitous and less susceptible to be poisoned. In addition, introducing carbon support can make up the poor electronic-conductivity of 3*d*-transition metal-based materials and then enhance the electron transfer rate[33, 34]. Heteroatom doped carbon nanomaterials are recognized as metal-free category catalysts for their high catalytic activity[7, 35, 36]. Numerous researches have demonstrated that the incorporation of non-precious *3d*-transition metal-based materials with various modified carbon materials would result in a synergistic effect for higher electrocatalytic performance and excellent electrochemical stability towards ORR and OER[37-40]. Moreover, thermal treatment conditions, modification of carbon support and metal species are also responsible for the electrocatalytic performance of the catalysts[41-44]. Porphyrin and phthalocyanine have been investigated as efficient chelating agents with transition metal salts in water solution and act as electrocatalysts for the improvement of ORR[45-48]. However, these chelating agents are reported with a relatively high price which impeded their further application. Other commonly used nitrogen sources (e.g. urea and NH_3) would not influence the morphology of the catalysts which is not conducive to in-depth exploration for the activity and durability of ORR and OER[49]. Thus, further investigation of nitrogen sources for the synthesis of nitrogen doped carbon supported *3d*-transition metal based catalysts with novelty structure and physical properties to improve the electrocatalytic performance is in active demand. Ethylenediamine tetra-acetic acid (EDTA), a common chelating agent which can strongly coordinate with metal and act as nitrogen sources, has attracted much attention in energy conversion. Bao and co-workers encapsulate CoNi nanoalloy (CoNi@NC) electrocatalysts by using Co^{2+}, Ni^{2+} and Na_4EDTA as precursor for high performance hydrogen evolution reaction (HER)[50]. Moon and co-workers developed the 3D graphene encapsulating Ni_2P nanoparticles (Ni_2P@mesoG) and 3D mesoporous graphene (mesoG) for high performance HER and bifunctional catalysts (ORR and OER), respectively, by using Ni_2(EDTA) as precursor[51,52].

Herein, nitrogen doped carbon supported Co@CoO, MnO and Ni@NiO nanoparticles were synthesized via a simple one-pot method derives from the complexing function of EDTA. EDTA acts not only as a chelating agent to disperse metal ions (M^{2+}), but also as reducing agent and nitrogen sources for heteroatom doping. After annealed in N_2 atmosphere, the resulting catalysts were covered by a carbon layer derived from the carbonization of EDTA. As a bi-functional electrocatalyst towards ORR and OER, Co@CoO/NDC-700 exhibited superior electrocatalytic activity and durability compared to Pt/C and Ir/C. Moreover, the optimal catalyst derived air electrode showed high power density and excellent charge-discharge durability for a homemade zinc-air battery.

Results and discussion

Nitrogen doped carbon supported Co@CoO, Ni@NiO and MnO nanoparticles were obtained via a simple one-pot strategy. As illustrated in Scheme 1, M-EDTA/C precursor was first synthesized via the chelating reaction and impregnation approach. After evaporation of solvent, the chelate compounds are uniformed distributed on the carbon supports.

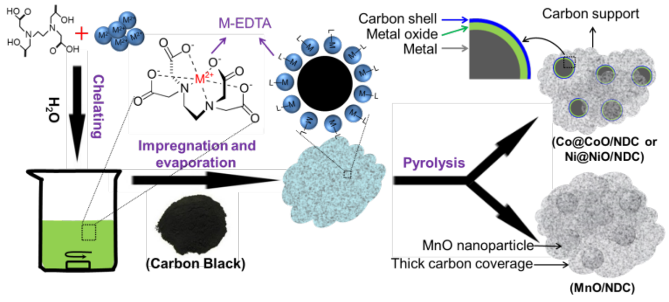

Scheme 1 Schematic illustration of the synthesis procedure for nitrogen doped carbon supported Co@CoO, Ni@NiO and MnO composites.

In the second step, the final products are obtained via high-temperature treatment of the precursor under flowing N_2 in a tube furnace. Based on different chelation strength of Mn^{2+},Co^{2+}, and Ni^{2+} with EDTA, the final products exhibited different physical characterization and electrochemical performance. The XRD patterns of Co@CoO/NDC-700, Ni@NiO/NDC-700, MnO/NDC-700 and NDC-700 are shown in FigS1a. The broad peak at around 25 ° is corresponding to (002) plane of carbon support. The diffraction peaks of Co@CoO/NDC-700 locate at 44.2 °, 51.5 °, 75.8 ° are corresponding to the (111), (200) and (220) lattice planes of Co, respectively, indicating the face-centered cubic (fcc) crystalline structure (JCPDS no. 89-4307). Besides, the diffraction peaks at 36.5 °, 42.4 °, 61.5 ° are attributed to the (111), (200) and (220) lattice planes of CoO, respectively. Similarly to Co@CoO/NDC-700, Ni@NiO/NDC-700 featured a fcc crystalline structure of Ni (JCPDS no. 65-0380) of (111), (200), (220) lattice planes located at 44.5 °, 51.8 ° and 76.4 °, respectively. Two additional diffraction peaks located at 37.4 ° and 63.1 ° are corresponding to the (111) and (220) lattice planes of NiO, respectively. The diffraction peaks of MnO/NDC-700 located at 35.0 °, 41.1 °, 58.6 °, 70.2 ° and 74.9 ° correspond to the (111), (200), (220) (311) and (222) crystal planes of MnO (JCPDS no. 78-0424), respectively. In comparison, the XRD patterns of Co/CoO/C, MnO_x/C and Ni/NiO/C (Fig. S1b) showed increased diffraction peak intensity of metal oxides relative to Fig. S1a, indicating the reductive property of EDTA. The thermal stability and specific content of the three catalysts are evaluated via TGA measurement (Fig. S2). It can be seen that the weight percentage of Co@CoO/NDC-700 and Ni@NiO/NDC-700 gradually increased from 350 °C and 380 °C with the increase of temperature, respectively, which would be explained by the transformation from metal into metal oxides. When the temperature was increased above 400 °C, a sharp weight loss was observed from the three catalysts due to the combustion of carbon. The weight percentage was stabilized at around 600 °C. According to the TGA curves, the final weight content of the three catalysts was approximately 20%.

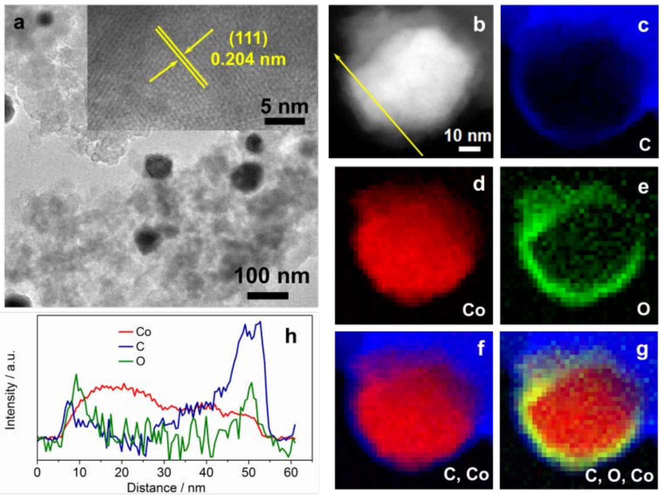

Fig. 1 (a) TEM images and HRTEM images (inset) of Co@CoO/NDC-700 nanoparticles; (b) DF-STEM image of one Co@CoO particle and the corresponding EELS elemental mapping of C (c), Co (d), O (e), C vs. Co (f) and composite (g); (h) EDX line profile of Co (red), C (blue) and O (green), showing the double-shell structure.

The morphology and physical characterization of the catalysts were investigated via TEM and DF-STEM equipped with EELS. Fig. 1a presents the overview TEM image of the particles with main diameter ranging from 40 to 50 nm (Fig. S4a). The inter-planar spacing between adjacent fringes is measured to be 0.204 nm from HRTEM image of an individual particle (inset of Fig. 1a) corresponding to (111) planes which is consistent with the inter-planar spacing calculated from the XRD patterns (Fig. S1a). DF-STEM image and corresponding EELS elemental mapping of a particle were performed in order to better understand the elemental composition and distribution. As can be seen from Fig. 1b, the particle shows a core-shell structure. The EELS elemental mapping of C, Co, O, and the composites in Fig. 1c-g indicate that the particle is partially oxidized and wrapped by a carbon surface layer (Fig. 1c-g), which demonstrated double-shell structure. EDX line profile (Fig. 1h) scanning from the particle in Fig. 1b further verified the double-shell structure of Co@CoO/NDC-700. The yellow arrow starts from one side which, in turn, exhibits C peak, O peak and a wide Co peak.

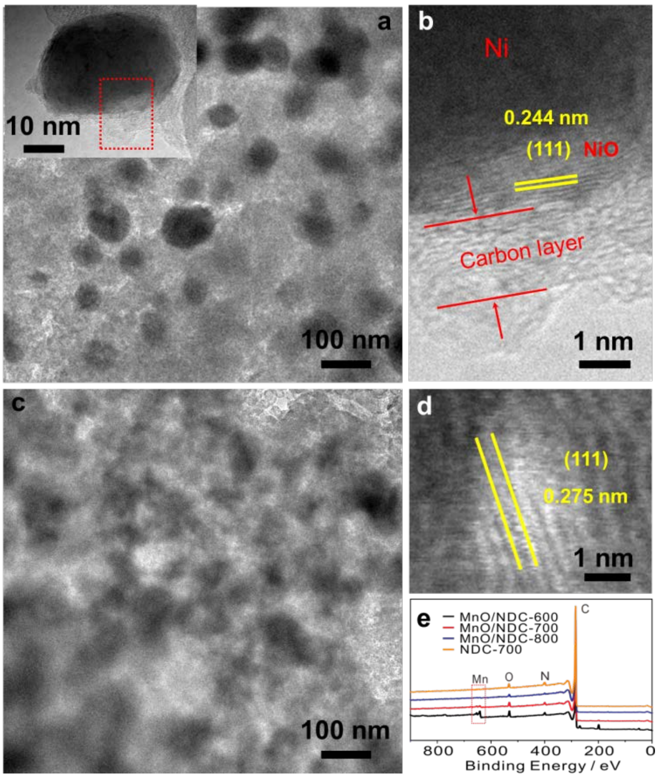

Fig. 2 (a) TEM image and the enlarged particle (inset) of Ni@NiO/NDC-700 nanoparticles; (b) HRTEM image of a partial Ni@NiO/NDC-700 particle in (a); TEM image (c), HRTEM image (d) of MnO/NDC-700 nanoparticles; (e) Full-range XPS image of MnO/NDC-600, MnO/NDC-700, MnO/NDC-800 and NDC-700.

TEM image of Ni@NiO/NDC-700 catalyst (Fig. 2a) showed a uniform distribution of nanoparticles with an average particle size ranging from 20 nm to 40 nm (Fig. S4b). The inset of Fig. 2a presents a Ni@NiO/NDC-700 particle with obvious layer coverage on the surface which is similar to the structure of Co@CoO/NDC-700. The HRTEM image (Fig. 2b) selected from the red dashed square border in Fig. 2a exhibited a two layer structure from the inner to the outside which presented an inter-planar spacing value of 0.244 nm, corresponding to (111) plane of NiO and carbon layer, respectively. As can be seen from the TEM image in Fig. 2c, the MnO/NDC-700 particles experienced thick carbon-coated structure and presented in blurred particle contour with an average particle size ranging from 30 to 50 nm (Fig. S4c) which is consistent with the Scherrer equation results of the XRD pattern in Fig. S1a. In addition, the carbon-coated structure was also confirmed via the full-range XPS image of MnO/NDC-600, MnO/NDC-700 and MnO/NDC-800 nanomaterials (Fig. 2d) annealed at 600 °C, 700 °C and 800 °C, respectively, for the XPS characterization is a surface analysis technique. As the increasing of annealing temperature, the intensity signal of Mn 2p peak gradually decreased due to the growing compact of carbon. HRTEM image in Fig. 2e shows obvious inter-planar spacing value of 0.275 nm between the two yellow adjacent fringe, corresponding to the (111) plane of MnO. Selected area electron diffraction pattern (SAED) in Fig. S5 revealed the strong crystallinity of the as synthesized spinel phase MnO with strong ring patterns diffracted by (111) plane and (200) plane.

In order to explain the formation mechanism of the double-shell structure, density functional theory (DFT) theoretical calculation of the charge density for every atom in Co-EDTA and EDTA was performed by using B3LYP method. It can be seen that after chelating reaction the six coordination bonds in Co-EDTA result in an EDTA encircle around Co^{2+} (Fig. S3). The value of mulliken atomic charge for O atom in Co-O bond decreased, while the value of N atom in Co-N bond becomes more positive, indicating strong bonding after forming the chelate compound. After annealing at high temperature, the Co atoms aggregated and forming nanoparticles, meanwhile, the chelating agent would be carbonized to form a carbon layer around the particle owing to the tight bonding. Besides, the surface Co atoms are likely to coordinate with O to form a CoO shell during the annealing process. According to the physical characterization and theoretical calculation results, it is concluded that the morphology of the as-prepared catalysts was determined by the $\lg K_{\text{M-EDTA}}$ ($\lg K_{\text{Co-EDTA}}$ = 16.3, $\lg K_{\text{Ni-EDTA}}$ = 18.6 and $\lg K_{\text{Mn-EDTA}}$ = 14.0), higher $\lg K$ value would result in core-shell structure, while the catalysts would be covered by thick carbon layer with relative low $\lg K$ value.

To further elucidate the bonding configurations and the surface elemental compositions, XPS characterization was conducted on Co@CoO/NDC-700, Ni@NiO/NDC-700, MnO/NDC-700 and NDC-700. As shown in the full-range XPS spectra in Fig. 3a, characteristic peaks of the corresponding elements for the above catalysts were observed. The specific elemental content for each catalyst was revealed in Table S2. Co@CoO/NDC-700 exhibited the highest N content (3.4 at. %) compared with MnO/NDC-700, Ni@NiO/NDC-700 and NDC-700. The lower metal (Co, Mn and Ni) contents compared with the real contents in TGA test revealed a dense carbon layer on the surface of the nanoparticles. The high-resolution spectra of Co $2p_{3/2}$ and $2p_{1/2}$ in Fig. 3b can be fitted into three components corresponding to metallic Co, Co^{2+} and the satellite peaks. Among them, deconvoluted peaks at 781.5 eV and 797.3 eV are corresponding to metallic Co, while peak at 783.6 eV and 798.8 eV can be assigned to the Co^{2+} state. Satellite peaks located at 787.4 eV and 803.8 eV are featured for CoO[53, 54]. Similar to Co@CoO/NDC-700, the high-resolution spectra of Ni $2p_{3/2}$ and $2p_{1/2}$ (Fig. S6b) were fitted into three components corresponding to metallic Ni (855.2 eV and 872.6 eV), Ni^{2+} (857.4 eV and 874.5 eV) and the satellite peaks (861.9

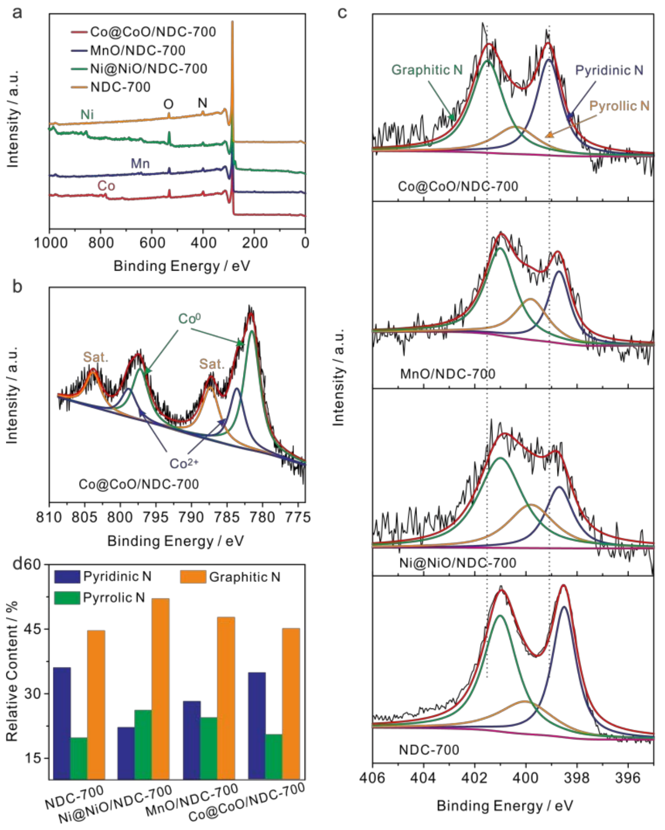

Fig. 3 (a) Full-range XPS spectrum of Co@CoO/NDC-700, MnO/NDC-700, Ni@NiO/NDC-700 and NDC-700; (b) High-resolution spectrum of Co 2p for Co@CoO/NDC-700; (c) High-resolution spectrum of N 1s for Co@CoO/NDC-700, MnO/NDC-700, Ni@NiO/NDC-700 and NDC-700; (d) Relative content of pyridinic N, pyrrolic N and graphitic N for the N 1s spectra in (c).

eV and 880.2 eV)[55], respectively. In addition, the high-resolution spectra of Mn $2p_{3/2}$ and $2p_{1/2}$ (Fig. S6a) were fitted into two components corresponding to Mn^{2+} (642.3 eV and 654.3 eV) and the satellite peaks (646.6 eV and 658.6 eV)[56], respectively. The resulting fitted peaks for the three catalysts are consistent with the XRD pattern in Fig. S1a. The high-resolution N1s spectrum (Fig. 3c) shows three single N species peaks for Co@CoO/NDC-700, MnO/NDC-700, Ni@NiO/NDC-700 and NDC-700 catalysts, corresponding to pyridinic N, pyrrolic N and graphitic N, respectively. In comparison to other catalysts, Co@CoO/NDC-700 shows an obvious N 1s peak shifting toward the higher binding energy which indicating a tight interaction between the CoO on the particle surface and doping N species. The relative content of N 1s species for the four catalysts which calculated from the deconvoluted peaks from Fig. 3c are shown in the histogram of Fig. 3d. Notably, the ORR activities are mainly relevant to pyridinic-N and graphitic-N which served as active sites[57-60]. Referring to the N 1s content in Table S2 and fitting N peaks in Fig. 3d, Co@CoO/NDC-700 exhibited the highest pyridinic-N and graphitic-N compared with other catalysts, coupled with the CoO-N interaction which are expected to exhibit synergistic effect for electrocatalytic performance[61].

The electrocatalytic activities of the as-prepared catalysts towards ORR were first assessed using cyclic voltammograms (CVs) in N_2- and O_2- saturated 1 M KOH solution with a potential range from 0.05 to 1.0 V (Fig. S7). It can be seen that obvious oxygen reduction peaks were presented when the electrolyte was saturated with O_2. Apparently, Co@CoO/NDC-700 exhibited pronounced ORR catalytic activity with a more positive peak potential (0.84 V) than MnO/NDC-700 (0.81 V), Ni@NiO/NDC-700 (0.77 V) and NDC-700 (0.78 V) catalysts. In addition, in order to investigate the bifunctional properties for the as-prepared catalysts, LSV measurements were recorded in O_2- saturated 1 M KOH solution in accordance with a potential range from 0.4 to 1.8 V (Fig. 4a). In detail, Co@CoO/NDC-700 exhibited excellent ORR performance with half-wave potential ($E_{1/2}$) of 0.85 V which is better than MnO/NDC-700 ($E_{1/2}$ = 0.83 V), Ni@NiO/NDC-700 ($E_{1/2}$ =0.75 V), NDC-700 ($E_{1/2}$ = 0.72V), Ir/C ($E_{1/2}$ = 0.79 V) and Pt/C ($E_{1/2}$ = 0.84 V). As for the polarization curves of the OER part, the current density of Ni@NiO/NDC-700 and Co@CoO/NDC-700 reach 10 mA cm^{-2} at 1.60 V and 1.62 V ($E_{j=10\ mA\ cm\text{-}2}$ represents a 10% efficient solar water-splitting device[62, 63]), respectively, which are much better than MnO/NDC-700 (1.70 V), NDC-700 (1.66 V) and Pt/C (1.67 V), but slightly inferior than Ir/C (1.57 V). To better understand the bifunctional performance of the as-prepared catalysts, the overall oxygen electrode activity is commonly evaluated by the difference value in potential (ΔE) between $E_{j=10\ mA\ cm\text{-}2}$ and $E_{1/2}$ from the bifunctional polarization curves of the as-prepared catalysts[64]. An ideal reversible oxygen electrode tends to exhibit a smaller ΔE. The ΔE for the as-prepared catalysts and the comparison of catalysts (Pt/C and Ir/C) was converted into histogram which can be seen from the inset of Fig. 4a. Co@CoO/NDC-700 exhibited a pronounced ΔE value of 0.76 V which is much lower than that of the as-prepared catalysts ($\Delta E_{MnO/NDC\text{-}700}$ = 0.88 V, $\Delta E_{Ni@NiO/NDC\text{-}700}$ = 0.85 V, $\Delta E_{NDC\text{-}700}$ = 0.94 V) and outperformed Pt/C (0.82 V) and Ir/C (0.78 V). In order to optimize the annealing temperature, the M-EDTA/C precursors annealed at 600 °C and 800 °C in N_2 atmosphere were also prepared. In terms of the polarization curves in Fig. S8, catalysts annealed at 700 °C exhibited the best bifunctional performance, whereas lower or higher the annealing temperature would result in inadequate carbonization of EDTA or relatively heteroatom N loss, respectively. In addition, the catalysts calcined at 700 °C without EDTA were also evaluated for their bifunctional performance (Fig. S9), in which the ORR and OER activities for the three catalysts were significantly decreased compared with Ni/@NiONDC-700, MnO/NDC-700 and Co@CoO/NDC-700 catalysts. Therefore, it is concluded that Co@CoO/NDC-700 exhibited the best bifunctional catalytic activity for the ORR and OER.

The Tafel plots for ORR and OER on different catalysts were performed to further investigate the electrode kinetics. As shown in Fig. 4b, the Tafel plots for the as-prepared catalysts were obtained by plotting the logarithm of the kinetic current density derived from the ORR polarization part in Fig. 4a. As a result, Co@CoO/NDC-700 and MnO/NDC-700 exhibited Tafel slope value of 42.7 mV dec^{-1} and 41.4 mV dec^{-1}, respectively, slightly lower than the value of 54.8 mV dec^{-1} on Pt/C,

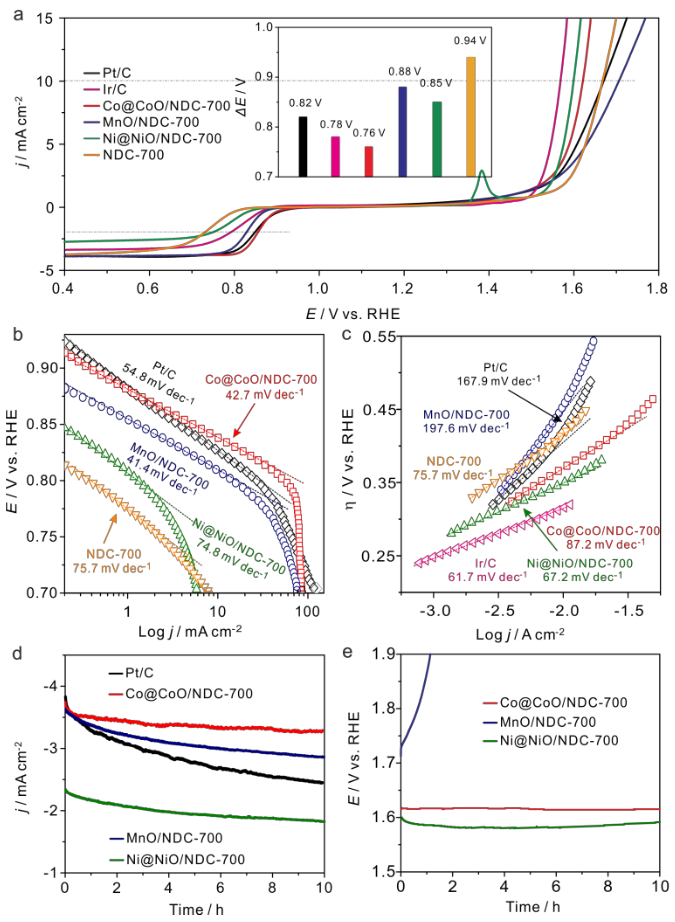

Fig. 4 (a) Bifunctional polarization curves on NDC-700, Ni@NiO/NDC-700, MnO/NDC-700, Co@CoO/NDC-700 and Pt/C in O_2-saturated 1 M KOH solution at scan rate of 5 mV s^{-1} and rotation rate of 1600 rpm; Corresponding Tafel plots of ORR polarization curves (b) and OER polarization curves (c); (d) I-t chronoamperometric stability measurement (at constant potential of 0.7 V) of Ni@NiO/NDC-700, MnO/NDC-700, Co@CoO/NDC-700 and Pt/C in O_2-saturated 1 M KOH solution at a rotating speed of 1600 rpm; (e) Chronopotentiometry curves of Ni@NiO/NDC-700, MnO/NDC-700 and Co@CoO/NDC-700, at a constant anodic current density of 10 mA cm^{-2} with a rotation rate of 1600 rpm.

indicating the protonation of O_2^{-} on the active sites of the catalyst is the main rate-determining step[65]. While the relative higher Tafel slope of NDC-700 (75.7 mV dec^{-1}) and Ni@NiO/NDC-700 (74.8 mV dec^{-1}) revealed lower catalytic rate. The Tafel plots for OER were constructed by plotting the logarithm of the kinetic current density derived from the OER polarization part in Fig. 4a. As can be seen from Fig. 4c, the Tafel slope of Ni@NiO/NDC-700 (67.2 mV dec^{-1}) is substantially equal to Ir/C (61.7 mV dec^{-1}), slightly lower than Co@CoO/NDC-700 (87.2 mV dec^{-1}) and much lower than those of MnO/NDC-700 (197.6 mV dec^{-1}), NDC-700 (95.7 mV dec^{-1}) and Pt/C (167.9 mV dec^{-1}), indicating excellent catalytic kinetics of Ni@NiO/NDC-700 and Co@CoO/NDC-700. Compared with the Tafel slope of ORR and OER, Co@CoO/NDC-700 exhibited incontrovertible catalytic kinetics which indicated the accelerating bifunctional catalytic reaction rates. To gain further insights into the ORR mechanism and the electron transfer pathway, rotating ring-disc voltammogram measurements was characterized for Co@CoO/NDC-700, MnO/NDC-700 and Ni@NiO/NDC-700 catalysts in O_2-saturated 1 M KOH solution. The ring current density curves for Co@CoO/NDC-700, MnO/NDC-700 and Ni@NiO/NDC-700 catalysts at a constant ring potential of 1.2 V are shown in Fig. S10a. Notably, Co@CoO/NDC-700 and MnO/NDC-700 exhibited much lower current density than Ni@NiO/NDC-700. Specifically, H_2O_2 production percentage and electron transfer number were calculated via equation (1) and (2), respectively. Results in Fig. S10b showed that Co@CoO/NDC-700 and MnO/NDC-700 yield substantially the same H_2O_2 production of ~ 5%, while for Ni@NiO/NDC-700 was more than 10 % with a potential range from 0.1 to 0.9 V. The 4-electron transfer number and low H_2O_2 production calculated from the aforementioned potential range for Co@CoO/NDC-700 and MnO/NDC-700 revealed a direct 4-electron pathway in the ORR process[33, 65].

The long-term catalytic stability of Ni@NiO/NDC-700, MnO/NDC-700 and Co@CoO/NDC-700 catalysts were assessed via chronoamperometric measurement for the ORR and chronopotentiometry for the OER. As shown in Fig. 4d, the Co@CoO/NDC-700 exhibits excellent ORR stability under a constant voltage of 0.7 V with maintaining a very slow attenuation over 10 h and retained 91.5% of the initial current, whereas MnO/NDC-700, Ni@NiO/NDC-700 and Pt/C showed nearly 20%, 20% and 35% loss of initial current, confirming the better ORR stability for Co@CoO/NDC-700. After ORR stability test, the particle size (Fig. 5a) showed slightly increase but maintained the double-shell structure. As can be seen from the elemental distribution images in Fig. 5(b-e), the thickness of CoO shell increased compared with Fig. 1(b-g), which indicates that the long-term stability test lead to slightly oxidation of Co core in Co@CoO/NDC-700. In addition, the ORR durability of Co@CoO/NDC-700 was also evaluated by accelerate potential cycling between 0.05 and 1.0 V in O_2-saturated 1 M KOH solution at a scan rate of 200 mV s^{-1}. As shown in Fig. S11, the Co@CoO/NDC-700 catalyst exhibited negligible oxygen reduction peak potential shift after 1000, 5000 and even 10,000 potential cycles, indicating superior catalytic stability. The OER durability of Ni@NiO/NDC-700, MnO/NDC-700 and Co@CoO/NDC-700 catalysts was conducted via chronopotentiometry measurement (Fig. 4e). Among the three catalysts, Ni@NiO/NDC-700 and Co@CoO/NDC-700 showed excellent potential stability at a constant current density of 10 mA cm^{-2} for over 10 h. Notably, the morphology of Co@CoO/NDC-700 still maintained the double-shell structure (Fig. 5f), even the oxidation degree of Co core further increased compared with the ORR stability test results, but the most of Co@CoO particles are still exist as metallic Co (Fig. 5g-j). Moreover, XRD characterization measurements were conducted for Co@CoO/NDC-700 catalyst after the durability tests by using a carbon paper electrode. As can be seen in Fig. S10, except the high diffraction intensity of carbon paper, diffraction peaks at 44.2 ° and 51.5 ° are

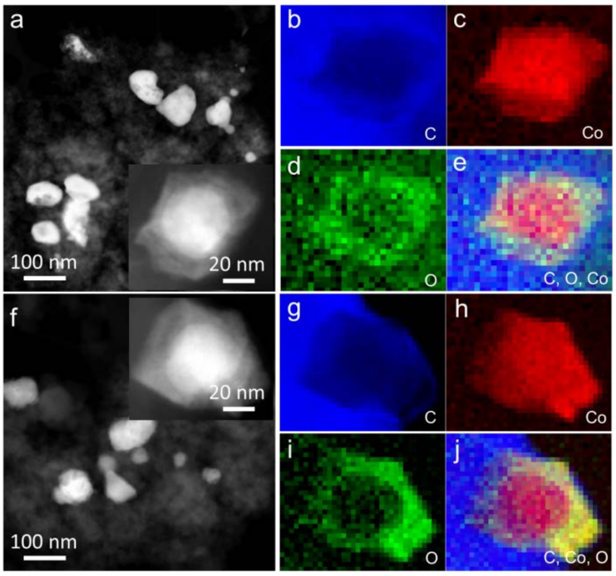

Fig. 5 (a) DF-STEM image of Co@CoO/NDC-700 after chronoamperometric stability measurement and one enlarged particle (inset) as well as the corresponding elemental mapping of C (b), Co (c), O (d) and the overlay of C, Co, O (e) elements. (f) DF-STEM image of Co@CoO/NDC-700 after chronopotentiometry stability measurement and one enlarged particle (inset) as well as the corresponding elemental mapping of C (g), Co (h), O (i) and the overlay of C, Co, O (j) elements.

correponding to the metallic Co, further confirming the existence of metallic Co core in Co@CoO/NDC-700 after durability test. Compared with the two XRD patterns (Fig. S12), the intensity of diffraction peaks for Co@CoO/NDC-700 catalyst after OER durability test is weaker which is attributed to the high working potential (~1.62 V) for OER facilitated the oxidation of metallic Co. The remarkable electrochemical stability and excellent catalytic selectivity of the Co@CoO/NDC-700 make it highly promising as a superior bifunctional oxygen electrocatalyst in Zn-air battery.

A homemade primary Zn-air battery by using the as-prepared catalysts as air electrode was constructed for further battery performance investigation (Fig. 6a). Fig. 6b presents the polarization and corresponding power density curves for Zn-air batteries. The Co@CoO/NDC-700 showed the highest current density of 324.1 mA cm^{-2} at potential of 0.6 V and a peak power density of ~192.1 mW cm^{-2} which is higher than Pt/C (268.0 mA cm^{-2} and 158.0 mW cm^{-2}), MnO/NDC-700 (251.1 mA cm^{-2} and 130.2 mW cm^{-2}) as well as Ni@NiO/NDC-700 (187.2 mA cm^{-2} and 109.5 mW cm^{-2}). The excellent performances of Co@CoO/NDC-700 originate from the unique structure and heteroatom doping which decreased the integrate resistance and increased the active sites. The Zn-air battery delivered a specific capacity of 736 mAh g_{Zn}^{-1} with high discharge platform of 1.31 V (Fig. 6c) for Co@CoO/NDC-700 and Pt/C at a current density of 5 mA cm^{-2}, corresponding to a 92.1 % utilization of the theoretical capacity (~820 mAh g_{Zn}^{-1}). Moreover, specific capacity of 701.2 mAh g_{Zn}^{-1} was obtained when the current density rose to 20 mA cm^{-2}. The excellent discharge capacities in both 5 mA cm^{-2} and 20 mA cm^{-2} indicate a good catalyst candidate for air-electrode in Zn-air battery. Fig. 6d exhibits the cycling stability of discharge/charge performance at a current density of 10 mA cm^{-2} for Co@CoO/NDC-700 and Pt/C. As can be seen that Co@CoO/NDC-700 maintained excellent cycling stability even after 100 h with a discharge/charge time step of 30 min with a near constant discharge/charge voltage gap of 0.68 V, while Pt/C suffers gradually discharge/charge platform loss after 25 h. Besides, compared with the discharge/charge platform and durability for the discharge/charge performance of MnO/NDC-700 (Fig. S13) and Ni@NiO/NDC-700 (Fig. S14), the Zn-air

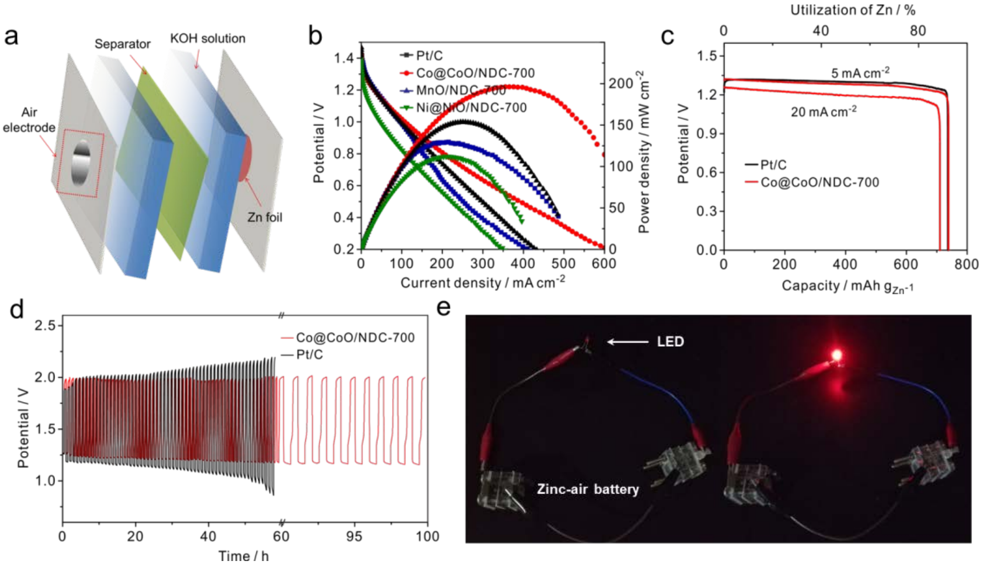

Fig. 6 (a) Schematic of a primary Zn–air battery; (b) Polarization and power density curves of primary Zn–air batteries; (c) Specific capacities of the Zn–air batteries by using Co@CoO/NDC-700 and Pt/C as air electrode catalysts (normalized to the mass of the consumed Zn); (d) Discharge/charge cycling curves of a three-electrode Zn–air battery using Co@CoO/NDC-700 and Pt/C at current density of 10 mA cm^{-2}; (e) Optical images of an LED (~2.2 V) before and after being driven by two Zn–air batteries.

battery using Co@CoO/NDC-700 as air electrode catalysts exhibited pronounced battery performance. These results illustrate the effective applicability of Co@CoO/NDC-700 as air cathode catalysts for Zn-air batteries, especially in the rechargeable form. Notably, two Zn-air batteries were connected in series to generate effective potential to power a ~2.2 V light-emitting diodes (LEDs) (Fig. 6e) The key battery performance parameters presented are ranked in the front row for the rechargeable Zn-air system listed in literatures (Table S3).

Conclusions

In conclusion, the nitrogen doped carbon supported Ni@NiO, MnO and Co@CoO catalysts have been successfully prepared via a simple one-pot synthetic method. The preparation procedure is simple, template- and surfactant-free, which is suitable for scalable production. The as-prepared catalysts were covered by a carbon layer derived from the carbonization of EDTA and the morphology was depending on the complex constant for M-EDTA. As a result, Co@CoO/NDC-700 have exhibited much better bifunctional performances towards ORR and OER than MnO/NDC-700, Ni@NiO/NDC-700, NDC-700, Pt/C and Ir/C, which are attributed to the synergistic effect between metal and nitrogen doped carbon. Due to the superior bifunctional properties, Co@CoO/NDC-700 exhibited promising cell performance as air catalysts in aqueous rechargeable Zn-air batteries.

Experimental

Material Synthesis

The preparation of Co@CoO/NDC composite is carried out as the following description: Firstly, $CoCl_2 \cdot 6H_2O$ (144.1 mg) and EDTA (212.7 mg) was added into a 50 mL beaker with 30 mL purified water. The mixture was then magnetic stirred at 85 °C along with ultrasonic dispersion until EDTA was completely reacted with Co^{2+} to form homogeneous solution. Subsequently, 160 mg of Vulcan XC-72 was dispersed into the solution along with ultrasonic dispersion and magnetic stirring at 85 °C for the evaporation of water to form thick slurry. The composite was then transferred into a vacuum oven at 50 °C overnight. After milling in an agate mortar, the resulting powder was annealed at 600 °C, 700 °C and 800 °C at a heating rate of 5 °C min^{-1} for 2 h under N_2 atmosphere. The resulting products were denoted as Co@CoO/NDC-600, Co@CoO/NDC-700 and Co@CoO/NDC-800, respectively.

The Ni@NiO/NDC and MnO/NDC composite were prepared by using the same method.

For comparison, Co/CoO/C, Ni/NiO/C and MnO_x/C catalysts were prepared by using the same method without adding EDTA. NDC-700 catalyst was prepared without adding metal salts.

Material Characterization

Powder X-ray diffraction (XRD) was performed by using an X'Pert PRO diffractometer, and diffraction patterns were collected at a scanning rate of 4 ° min^{-1}. Thermal gravimetric analysis (TGA) was conducted on TA Q500 Instrument from room temperature to 800 °C at a heating rate of 10 °C min^{-1}. X-ray photoelectron spectroscopy (XPS) data were obtained using an AXIS-ULTRA DLD-600W Instrument. Transmission electron microscopy (TEM), dark field scanning transmission electron microscopy (DF-STEM) and high-resolution transmission electron microscopy images (HRTEM) were obtained using 200 and 300 keV field-emission S/TEMs. Electron Energy Loss Spectroscopy (EELS) data were acquired by using a Gatan Tridiem spectrometer. The theoretical calculations presented were performed using the density functional B3LYP as implemented in the Gaussian 09 program.

Electrochemical Measurements

The electrochemical measurements were performed at room temperature using a three-electrode system comprising a carbon rod counter electrode, reverse hydrogen electrode (RHE) reference electrode and catalyst modified rotating disk glass-carbon working electrode (RDE, disk diameter 5 mm) or rotating ring-disc glass-carbon working electrode (RRDE, disk diameter 5 mm, ring inside diameter 6.25 mm, outside diameter 7.92 mm). Typical for prepared the working electrode, 5 mg of catalyst was ultrasonically dispersed into 1 mL isopropanol/Nafion hybrid solution to form homogeneous ink. Subsequently, 16 μL of ink (21 μL for RRDE) is dropped onto the glass-carbon substrate, and dried naturally. In comparison, the loading of Pt on the glassy carbon is ca. 15 μg cm^{-2}. Autolab PGSTAT302N electrochemical workstation equipped with a high speed rotator from Pine Instruments was used to measure the electrochemical performance. 1 M KOH solution was employed as electrolyte which was pre-purged with N_2 or O_2 for at least 30 min before each test and maintained gas flow until the end of the tests. The scan rate of cyclic voltammograms (CVs) was kept at 50 mV s^{-1} from 0.05 to 1.0 V. The linear sweep voltammograms (LSVs) was performed at a scanning rate of 5 mV s^{-1}, and the ring potential was constant at 1.2 V vs. RHE for RRDE measurements. The electron transfer number (n) was calculated from the rotating ring-disc voltammogram via the following equation (1), while the hydrogen peroxide production can be calculated from equation (2).

$$n = \frac{4 j_D}{j_D + \frac{j_R}{N}} \tag{1}$$

$$H_2O_2\% = \frac{\frac{2 j_R}{N}}{j_D + \frac{j_R}{N}} \times 100\% \tag{2}$$

Rechargeable Zn-air batteries performance was tested in homemade electrochemical cells. A two-electrode configuration was used by pairing the as-prepared catalyst loaded on a gas-diffusion electrode (1 cm^2, catalyst loading 1 mg cm^{-2}) with a pre-polished Zn foil in 2 mL of 6 M KOH with 0.2 M $Zn(CH_3COO)_2$. The preparation of gas-diffusion electrode is as follows: 400 mg of Vulcan XC-72 and 100 mg PTFE were fully milled in agate mortar with moderate isopropanol to form homogenous slurry. Subsequently, the slurry was rolled into a 3 mm thick sheet in a roll machine. After drying in a vacuum oven and the gas-diffusion electrode was obtained by tailoring into suitable size. The LAND-CT2001A testing devices were used to analyze the discharge/charge performance with air continuously fed to the cathode during battery measurements.

Acknowledgements

This work was supported by the National Natural Science Foundation (21573083), the Program for New Century Excellent Talents in Universities of China (NCET-13-0237), the Fundamental Research Funds for the Central University (2013TS136, 2014YQ009), 1000 Young Talent (to Deli Wang), and initiatory financial support from Huazhong University of Science and Technology (HUST). The authors thank the Analytical and Testing Center of HUST for XRD, STEM measurements. S/TEM and EELS work was carried out at the Center for Functional Nanomaterials, Brookhaven National Laboratory, which is supported by the U.S. Department of Energy, Office of Basic Energy Sciences, under Contract No. DE-SC0012704.

Notes and references

1 G. Wu, K. L. More, C. M. Johnston and P. Zelenay, *Science*, 2011, **332**, 443.
2 M. A. Rahman, X. Wang and C. Wen, *J. Electrochem. Soc.*, 2013, **160**, A1759.
3 D. Wang, H. L. Xin, R. Hovden, H. Wang, Y. Yu, D. A. Muller, F. J. DiSalvo and H. D. Abruña, *Nat. Mater.*, 2013, **12**, 81.
4 R. Silva, D. Voiry, M. Chhowalla and T. Asefa, *J. Am. Chem. Soc.*, 2013, **135**, 7823.
5 H.-W. Liang, W. Wei, Z.-S. Wu, X. Feng and K. Müllen, *J. Am. Chem. Soc.*, 2013, **135**, 16002.
6 C. Zhang, N. Mahmood, H. Yin, F. Liu and Y. Hou, *Adv. Mater.*, 2013, **25**, 4932.
7 J. Jin, F. Pan, L. Jiang, X. Fu, A. Liang, Z. Wei, J. Zhang and G. Sun, *ACS Nano*, 2014, **8**, 3313.
8 W.-H. Ryu, T.-H. Yoon, S. H. Song, S. Jeon, Y.-J. Park and I.-D. Kim, *Nano Lett.*, 2013, **13**, 4190.
9 Y.-C. Lu, H. A. Gasteiger and Y. Shao-Horn, *J. Am. Chem. Soc.*, 2011, **133**, 19048.
10 Y. Li, M. Gong, Y. Liang, J. Feng, J.-E. Kim, H. Wang, G. Hong, B. Zhang and H. Dai, *Nat. Commun.*, 2013, **4**, 1805.
11 J. Y. Cheon , K. Kim , Y. J. Sa , S. H. Sahgong , Y. Hong , J. Woo , S.-D. Yim , H. Y. Jeong , Y. Kim, S. H. Joo, *Adv. Energy Mater.*, 2016, **6**, 1501794.
12 S. Dou , X. Li , L. Tao, J. Huo, S. Wang, *Chem. Commun.*, 2016, **52**, 9727.
13 B. Lim, M. Jiang, P. H. Camargo, E. C. Cho, J. Tao, X. Lu, Y. Zhu and Y. Xia, *Science*, 2009, **324**, 1302.
14 X. Wang, L. Figueroa-Cosme, X. Yang, M. Luo, J. Liu, Z.-x. Xie and Y. Xia, *Nano Lett.*, 2016, **16**, 1467.
15 P. Strasser and S. Kühl, *Nano Energy*, 2016, **29**, 166.
16 A. S. Aricò, P. Bruce, B. Scrosati, J.-M. Tarascon and W. Van Schalkwijk, *Nat. Mater.*, 2005, **4**, 366.
17 R. Ning, J. Tian, A. M. Asiri, A. H. Qusti, A. O. Al-Youbi and X. Sun, *Langmuir*, 2013, **29**, 13146.
18 M. K. Debe, *Nature*, 2012, **486**, 43.
19 H. W. Park, D. U. Lee, P. Zamani, M. H. Seo, L. F. Nazar and Z. Chen, *Nano Energy*, 2014, **10**, 192.
20 Y. Lee, J. Suntivich, K. J. May, E. E. Perry and Y. Shao-Horn, *J. Phys. Chem. Lett.*, 2012, **3**, 399.
21 Y. J. Sa, K. Kwon, J. Y. Cheon, F. K. and S. H. Joo, *J. Mater. Chem. A*, 2013, **1**, 9992.
22 T. Y. Ma, S. Dai, M. Jaroniec, S. Z. Qiao, *J. Am. Chem. Soc.*, 2014, **136**, 13925.
23 J. Zhang, Z. Zhao, Z. Xia, L. Dai, *Nat. Nanotechnol.*, 2015, **10**, 444.
24 T. Maiyalagan, *K. A. Jarvis, S. Therese, P. J. Ferreira, A. Manthiram, Nat. Commun.*, 2014, **5**, 3949.
25 B. Seo, Y. J. Sa, J. Woo, K. Kwon, J. Park, T. J. Shin, H. Y. Jeong, S. H. Joo, *ACS Catal.*, 2016, **6**, 4347.
26 S. Dou, L. Tao, J. Huo, S. Wang, L. Dai, *Energy Environ. Sci.*, 2016, **9**, 1320.
27 J. Xu, P. Gao and T. S. Zhao, *Energy Environ. Sci.*, 2012, **5**, 5333.
28 S. Guo, S. Zhang, L. Wu and S. Sun, *Angew. Chem.*, 2012, **51**, 11770.
29 Z. Jiang, Z.-J. Jiang, T. Maiyalagan and A. Manthiram, *J. Mater. Chem. A*, 2016, **4**, 5877.
30 A. Indra, P. W. Menezes, N. R. Sahraie, A. Bergmann, C. Das, M. Tallarida, D. Schmeißer, P. Strasser and M. Driess, *J. Am. Chem. Soc.*, 2014, **136**, 17530.
31 Y. Zhao, R. Nakamura, K. Kamiya, S. Nakanishi, K. Hashimoto, *Nat. Commun.* 2013, **4**, 2390.
32 N. R. Sahraie, J. P. Paraknowitsch, C. Göbel, A. Thomas, P. Strasser, *J. Am. Chem. Soc.* 2014, **136**, 14486.
33 J. Wang, Z. Wu, L. Han, R. Lin, W. Xiao, C. Xuan, H. L. Xin and D. Wang, *J. Mater. Chem. A*, 2016, **4**, 5678.
34 H. B. Wu, G. Zhang, L. Yu and X. W. D. Lou, *Nanoscale Horizons*, 2016, **1**, 27.
35 T. Xing, Y. Zheng, L. H. Li, B. C. C. Cowie, D. Gunzelmann, S. Z. Qiao, S. Huang and Y. Chen, *ACS Nano*, 2014, **8**, 6856.
36 K. Qu, Y. Zheng, S. Dai and S. Z. Qiao, *Nano Energy*, 2016, **19**, 373.
37 Y. Liang, Y. Li, H. Wang, J. Zhou, J. Wang, T. Regier and H. Dai, *Nat. Mater.*, 2011, **10**, 780.
38 Z. Xiang, Y. Xue, D. Cao, L. Huang, J. F. Chen and L. Dai, *Angew. Chem. Int. Ed.*, 2014, **53**, 2433.
39 M. Lefèvre, E. Proietti, F. Jaouen and J.-P. Dodelet, *Science*, 2009, **324**, 71.
40 Z. Wu, J. Wang, L. Han, R. Lin, H. L. Xin, H. Liu and D. Wang, *Nanoscale*, 2016, **8**, 4681.
41 C. W. Bezerra, L. Zhang, K. Lee, H. Liu, A. L. Marques, E. P. Marques, H. Wang and J. Zhang, *Electrochim. Acta*, 2008, **53**, 4937.
42 F. Zhao, F. Harnisch, U. Schröder, F. Scholz, P. Bogdanoff and I. Herrmann, *Electrochem. Commun.*, 2005, **7**, 1405.
43 D. H. Lee, W. J. Lee, W. J. Lee, S. O. Kim and Y.-H. Kim, *Phys. Rev. Lett.*, 2011, **106**, 175502.
44 R. Bashyam and P. Zelenay, *Nature*, 2006, **443**, 63.
45 R. Chen, H. Li, D. Chu and G. Wang, *J. Phys. Chem. C*, 2009, **113**, 20689.
46 L. Wu, Y. Nabae, S. Moriya, K. Matsubayashi, N. M. Islam, S. Kuroki, M.-a. Kakimoto, J.-i. Ozaki and S. Miyata, *Chem. Commun.*, 2010, **46**, 6377.
47 S. Baranton, C. Coutanceau, C. Roux, F. Hahn and J.-M. Leger, *J. Electroanal. Chem.*, 2005, **577**, 223.
48 W. Li, A. Yu, D. C. Higgins, B. G. Llanos and Z. Chen, *J. Am. Chem. Soc.*, 2010, **132**, 17056.
49 Q. Lv, H. Sun, X. Li, J. Xiao, F. Xiao, L. Liu, J. Luo and S. Wang, *Nano Energy*, 2016, **21**, 39.
50 J. Deng, P. Ren, D. Deng, and X. Bao, *Angew. Chem. Int. Ed.*, 2015, **54**, 2100.
51 S. Jeoung, B. Seo, J. Hwang, S. H. Joo and H. R. Moon, *Mater. Chem. Front.*, 2017, DOI: 10.1039/C6QM00269B.

52 K. J. Lee, Y. J. Sa, H. Y. Jeong, C. W. Bielawski, S. H. Joo, *Chem. Commun.*, 2015, **51**, 6773.

53 X. Zhang, R. Liu, Y. Zang, G. Liu, G. Wang, Y. Zhang, H. Zhang and H. Zhao, *Chem. Commun.*, 2016, **52**, 5946.

54 R. Huo, W.-J. Jiang, S. Xu, F. Zhang and J.-S. Hu, *Nanoscale*, 2014, **6**, 203.

55 M. Yu, W. Wang, C. Li, T. Zhai, X. Lu and Y. Tong, *NPG Asia Mater.*, 2014, **6**, e129.

56 C.-H. Kuo, I. M. Mosa, S. Thanneeru, V. Sharma, L. Zhang, S. Biswas, M. Aindow, S. P. Alpay, J. F. Rusling and S. L. Suib, *Chem. Commun.*, 2015, **51**, 5951.

57 M. Li, L. Zhang, Q. Xu, J. Niu and Z. Xia, *J. Catal*, 2014, **314**, 66.

58 D. Geng, Y. Chen, Y. Chen, Y. Li, R. Li, X. Sun, S. Ye and S. Knights, *Energy Environ. Sci.*, 2011, **4**, 760.

59 L. Lai, J. R. Potts, D. Zhan, L. Wang, C. K. Poh, C. Tang, H. Gong, Z. Shen, J. Lin and R. S. Ruoff, *Energy Environ. Sci.*, 2012, **5**, 7936.

60 H. Yu, L. Shang, T. Bian, R. Shi, G. I. Waterhouse, Y. Zhao, C. Zhou, L. Z. Wu, C. H. Tung and T. Zhang, *Adv. Mater.*, 2016, **28**, 5080.

61 J. Masa, W. Xia, I. Sinev, A. Zhao, Z. Sun, S. Grützke, P. Weide, M. Muhler and W. Schuhmann, *Angew. Chem. Int. Ed.*, 2014, **53**, 8508.

62 M. F. Weber and M. J. Dignam, *J. Electrochem. Soc.*, 1984, **131**, 1258.

63 Y. Gorlin and T. F. Jaramillo, *J. Am. Chem. Soc.*, 2010, **132**, 13612.

64 T. Y. Ma, J. Ran, S. Dai, M. Jaroniec and S. Z. Qiao, *Angew. Chem. Int. Ed.*, 2015, **54**, 4646.

65 V. Stamenkovic, T. Schmidt, P. Ross and N. Markovic, *J. Phys. Chem. B*, 2002, **106**, 11970.